

Journal of Geophysical Research: Oceans

RESEARCH ARTICLE

10.1002/2015JC010805

Key Points:

- Evidence of upwelling around grounded tabular icebergs
- Upwelling causes cooling of the thermocline
- Evidence of differential disintegration on opposing sides of the iceberg

Supporting Information:

- Supporting Information S1
- Supporting Information S2
- Supporting Information S3
- Figure S1
- Figure S2
- Figure S3
- Table S1
- Table S2
- Software S1

Correspondence to:

A. A. Stern,
alon@cims.nyu.edu

Citation:

Stern, A. A., et al. (2015), Wind-driven upwelling around grounded tabular icebergs, *J. Geophys. Res. Oceans*, 120, 5820–5835, doi:10.1002/2015JC010805.

Received 25 FEB 2015

Accepted 14 JUL 2015

Accepted article online 17 JUL 2015

Published online 24 AUG 2015

Corrected 28 SEP 2015

This article was corrected on 28 SEP 2015. See the end of the full text for details.

Wind-driven upwelling around grounded tabular icebergs

Alon A. Stern¹, Eric Johnson¹, David M. Holland¹, Till J.W. Wagner², Peter Wadhams³, Richard Bates⁴, E. Povl Abrahamsen⁵, Keith W. Nicholls⁵, Anna Crawford⁶, Jonathan Gagnon⁷, and Jean-Eric Tremblay⁷

¹Courant Institute of Mathematical Sciences, New York University, New York, New York, USA, ²Scripps Institution of Oceanography, University of California San Diego, San Diego, California, USA, ³Department of Applied Mathematics and Theoretical Physics, University of Cambridge, Cambridge, UK, ⁴School of Geography and Geosciences, University of St. Andrews, Saint Andrews, UK, ⁵British Antarctic Survey, NERC, Cambridge, UK, ⁶Department of Geography and Environmental Studies, Carleton University, Ottawa, Ontario, Canada, ⁷Département de biologie et Québec-Océan, Université Laval, Québec City, Québec, Canada

Abstract Temperature and salinity data collected around grounded tabular icebergs in Baffin Bay in 2011, 2012, and 2013 indicate wind-induced upwelling at certain locations around the icebergs. These data suggest that along one side of the iceberg, wind forcing leads to Ekman transport away from the iceberg, which causes upwelling of the cool saline water from below. The upwelling water mixes with the water above the thermocline, causing the mixed layer to become cooler and more saline. Along the opposite side of the iceberg, the surface Ekman transport moves towards the iceberg, which causes a sharpening of the thermocline as warm fresh water is trapped near the surface. This results in higher mixed layer temperatures and lower mixed layer salinities on this side of the iceberg. Based on these in situ measurements, we hypothesize that the asymmetries in water properties around the iceberg, caused by the opposing effects of upwelling and sharpening of the thermocline, lead to differential deterioration around the iceberg. Analysis of satellite imagery around iceberg PII-B-1 reveals differential decay around the iceberg, in agreement with this mechanism.

1. Introduction

Large icebergs, which calve off outlet glaciers in Antarctica and Greenland, transport fresh water from the cryosphere into the global ocean. Driven by winds and currents, these massive pieces of ice drift away from their calving origins, ending up in regions with warmer water where they melt, break up and eventually dissolve completely. The trajectories and life cycles of the icebergs determine the spatial and temporal distribution of much of the fresh water flux from the cryosphere into the ocean, which is a nonnegligible term in the regional fresh water budget [Gladstone *et al.*, 2001; Silva *et al.*, 2006]. This has implications for various processes in the climate system, such as sea-ice distribution and, in Antarctica, bottom water formation [Dinniman *et al.*, 2007; Jongma *et al.*, 2009; Kusahara *et al.*, 2011; Robinson and Williams, 2012]. Icebergs can also affect the iron and nutrient levels locally, leading to the creation of biological hotspots [Kaufmann *et al.*, 2011; Vernet *et al.*, 2011, 2012; Smith, 2011; Biddle *et al.*, 2015] and increased sequestration of organic carbon to the deep ocean [Smith *et al.*, 2007; Shaw *et al.*, 2011].

The recent decline in Arctic summer sea ice extent has led to an increased usage of the Arctic for commercial shipping, as well as renewed efforts in hydrocarbon exploration in the region [Smith and Stephenson, 2013; Hossain and Rao, 2014]. The threat that icebergs still pose to ships and offshore structures continues to fuel interest in iceberg trajectories and decay mechanisms [Halliday *et al.*, 2012; Peterson *et al.*, 2012; Turnbull *et al.*, 2015]. Similarly, recent efforts to couple numerical ocean models to land-ice models have led to an increased interest in Arctic and Antarctic icebergs [Martin and Adcroft, 2010; Hunke and Comeau, 2011; Google, 2013]. While some progress has been made towards including icebergs in comprehensive climate models in recent years, hydrographic aspects of model simulations are difficult to constrain because of the scarcity of observational data. As a result, modeled iceberg distributions and trajectories are typically compared with iceberg data collected from satellite altimetry [Bigg *et al.*, 1997; Kehouche *et al.*, 2009; Martin and Adcroft, 2010; Hunke and Comeau, 2011]. In situ measurements of iceberg behavior are much rarer, due

to the inherent difficulties of collecting such data. This lack of field measurements has hindered our understanding of mechanical and thermodynamic processes that affect the iceberg life cycle.

This article is concerned with grounded icebergs and the processes that affect their decay, particularly in warm surface waters. Such processes include direct melting, forced convection caused by ocean velocities relative to the iceberg motion [Savage, 2001], wave-induced flexural stresses [Wadhams *et al.*, 1983], and what has been referred to as the “footloose” mechanism [Wagner *et al.*, 2014]. The latter is characterized by increased erosion at the sides of the iceberg due to warm water above the thermocline that can lead to the development of an ice foot below the thermocline, which exerts a strong hydrostatic buoyancy force on the edge of the iceberg, and eventually causes the iceberg edge to break off [Scambos *et al.*, 2005; Wagner *et al.*, 2014].

The grounding of an iceberg can also significantly affect its decay process. The initial impact caused by an iceberg hitting the sea floor as it runs aground can result in the iceberg breaking up and lead to an overall expedited decay [Martin *et al.*, 2010]. Once grounded, the iceberg will be subject to increased flexural stresses, induced by tidal forcing. Conversely, a grounded iceberg will also affect the ocean surrounding it, which in turn can either inhibit or enhance degradation. Firstly, the meltwater from grounded or ungrounded icebergs has the potential to either stabilize or destabilize the water column depending on the local hydrography [Neshyba, 1977; Donaldson, 1978; Gladstone *et al.*, 2001; Kubat *et al.*, 2007]. Buoyant subsurface meltwater can rise up the side of the iceberg either as a thin boundary layer, spreading a cool fresh water layer on the ocean surface [Helly *et al.*, 2011], or as a density plume, entraining ambient water, and resulting in density anomalies throughout the upper water column [Stephenson *et al.*, 2011]. The sign of this density anomaly depends on the ambient stratification and the amount of entrainment [Jenkins, 1999]. Alternatively, a neutrally buoyant meltwater plume can spread horizontally at depth, causing steps in the temperature and salinity profiles, which are maintained by the effects of double diffusion [Huppert and Turner, 1980; Stephenson *et al.*, 2011].

Grounded icebergs also affect the surrounding ocean by disrupting flow, thereby changing the general circulation patterns around the iceberg [Nøst and Østerhus, 1998; Grosfeld *et al.*, 2001; Robinson *et al.*, 2010]. In this way, grounded icebergs can act in a similar fashion to islands that are temporarily placed in the flow. Much work has been done on the effect of flow disruptions, wake vortices and upwelling/downwelling caused by the presence of small islands [e.g., Takahashi *et al.*, 1980; Wolanski *et al.*, 1996; Dietrich *et al.*, 1996; White *et al.*, 2008]. Insights gained through this work can be applied to the study of the circulation patterns around temporarily grounded icebergs. Of particular relevance here is the wind-driven upwelling and downwelling that is commonly observed along coastlines of continents and islands [Garvine, 1971; Takahashi *et al.*, 1980; De Szoeke and Richman, 1981; Bakun, 1990; Kämpf *et al.*, 2004]. Coastal upwelling occurs when wind-driven currents are directed offshore and are replenished by water from below. Such upwelling is often associated with increased biological productivity, as nutrient-rich water is brought to the surface [Hutchins and Bruland, 1998; Botsford *et al.*, 2003, 2006]. Similarly, coastal downwelling occurs when wind-driven onshore surface currents cause surface water to pile up against the coast and can then be forced downwards. In the northern hemisphere the wind-driven surface current takes the form of a surface Ekman transport that runs at 90° to the right of the prevailing wind direction [Ekman, 1905; Price *et al.*, 1987]. A northward wind along the east coast of a land mass, for example, will drive an eastward Ekman transport away from the coast, and result in upwelling. Changes to the prevailing wind direction drive changes in the upwelling signal after some adjustment time [Send *et al.*, 1987].

In this study, temperature and salinity measurements are presented from the water columns surrounding two grounded tabular Arctic icebergs, collected over three field seasons. These data suggest that a grounded iceberg can experience upwelling on one side and a sharpening of the density gradients at the base of the thermocline on the opposite side. Among other things, this upwelling and thermocline gradient sharpening affects the temperature of the thermocline around the iceberg, which has implications for the eventual iceberg decay (see schematic in Figure 1). The observed upwelling is driven by surface winds and is distinct from the previously observed upwelling along the sides of an iceberg driven by buoyant meltwater plumes [Neshyba, 1977; Helly *et al.*, 2011; Stephenson *et al.*, 2011].

The article is organized as follows: section 2 discusses details of the three field experiments and the instruments and methods used to collect and analyze these ocean data. Section 3 presents results from these

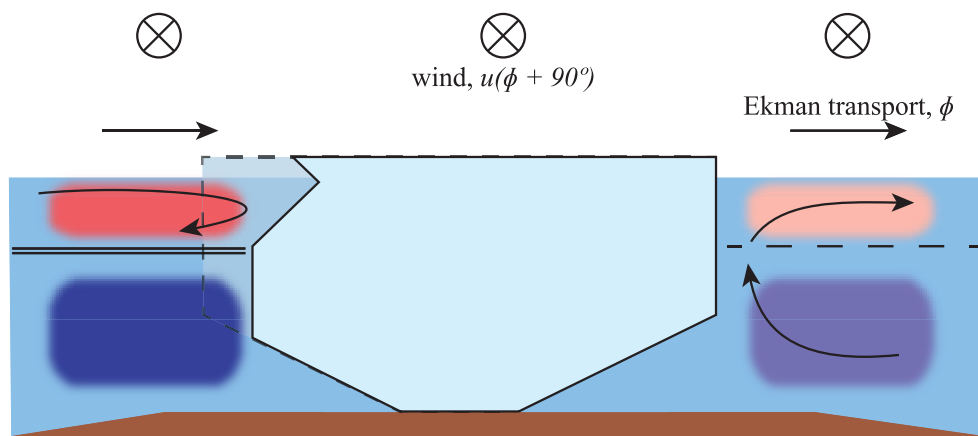


Figure 1. Schematic of the mechanism causing asymmetries in the mixed layer around grounded icebergs. Surface transport away from the iceberg to the right of the wind direction (in the northern hemisphere) causes upwelling on this side of the iceberg. The upwelling water causes the mixed layer to become cooler and more saline. On the opposite side of the iceberg (to the left of the wind direction in the northern hemisphere), the wind drives a surface transport towards the iceberg. Warm fresh water piles up against the iceberg, which causes a sharpening of the gradients at the base of the thermocline. This causes the mixed layer to be anomalously warm and fresh on this side of the iceberg. The warm fresh water in the thermocline drives preferential deterioration on this side of the iceberg through surface melting, and as a knock on effect through the footloose mechanism [Wagner et al., 2014].

three field experiments and shows the presence of asymmetries in the observed upper ocean temperatures and salinities around the icebergs. Section 4 contains a discussion of the observed results. Here we suggest that these upper-ocean asymmetries are caused by the presence of upwelling regions and regions of enhanced stratification on opposing sides of the icebergs. We further suggest that the increased surface water temperatures in the enhanced stratification regions may lead to an increased rate of iceberg degradation on one side of the iceberg. Section 5 contains some concluding remarks.

Note that in the Arctic, large tabular icebergs are commonly referred to as “ice islands,” however in this article we will use the term “icebergs” interchangeably.

2. Methods

2.1. Description of Field Work

Petermann Ice Island (PII) calved off Petermann Glacier in northwest Greenland on 8 August 2010. At the time of calving, PII had a surface area of 253 km^2 and was the largest Greenlandic calving event on record [Falkner et al., 2011]. Within a month of calving, two large collision events caused PII to split into 4 parts, the largest of which was PII-B. On 26 October 2010, three smaller fragments calved off of PII-B. These were named PII-B-a, PII-B-b and PII-B-c. The collision and fracture events were observed using RADARSAT-2 satellite imagery. After these fracture events, the remainder of PII-B continued to drift southwards along the western edge of Baffin Bay before becoming grounded on the continental shelf of Baffin Island on 18 June 2011, at $69^{\circ}38'N, 65^{\circ}52'W$, 130 km south east of Clyde River. Figure 2 shows the grounding position of PII-B, as well as (a) the regional and (b) the local bathymetry around the iceberg.

PII-B was first visited in October 2011. At this time, the iceberg had a surface area of 60 km^2 . Ocean CTD data were collected around PII-B on 20 October 2011. Three CTD casts were collected on both the southern side of the iceberg (200 m, 400 m, and 600 m from the iceberg edge) and the northern side of the iceberg (200 m, 300 m, and 400 m from the iceberg edge). One cast was collected on both the western and eastern sides of the iceberg, at approximately 300 m and 400 m from the iceberg edge, respectively. During this expedition, wind data were collected in situ by a wind monitor positioned on the ship ~ 15 m above the water line, and later corrected for the ship motion.

On 13 November 2011, PII-B split into two parts. While the smaller part, PII-B-2, drifted southwards, the larger part, PII-B-1, remained grounded at the same location. PII-B-1 was visited for a second time in July 2012 as part of a wider field campaign performed in conjunction with the British Broadcasting Corporation (BBC). Some results from this field campaign are presented in the BBC television documentary *Operation*

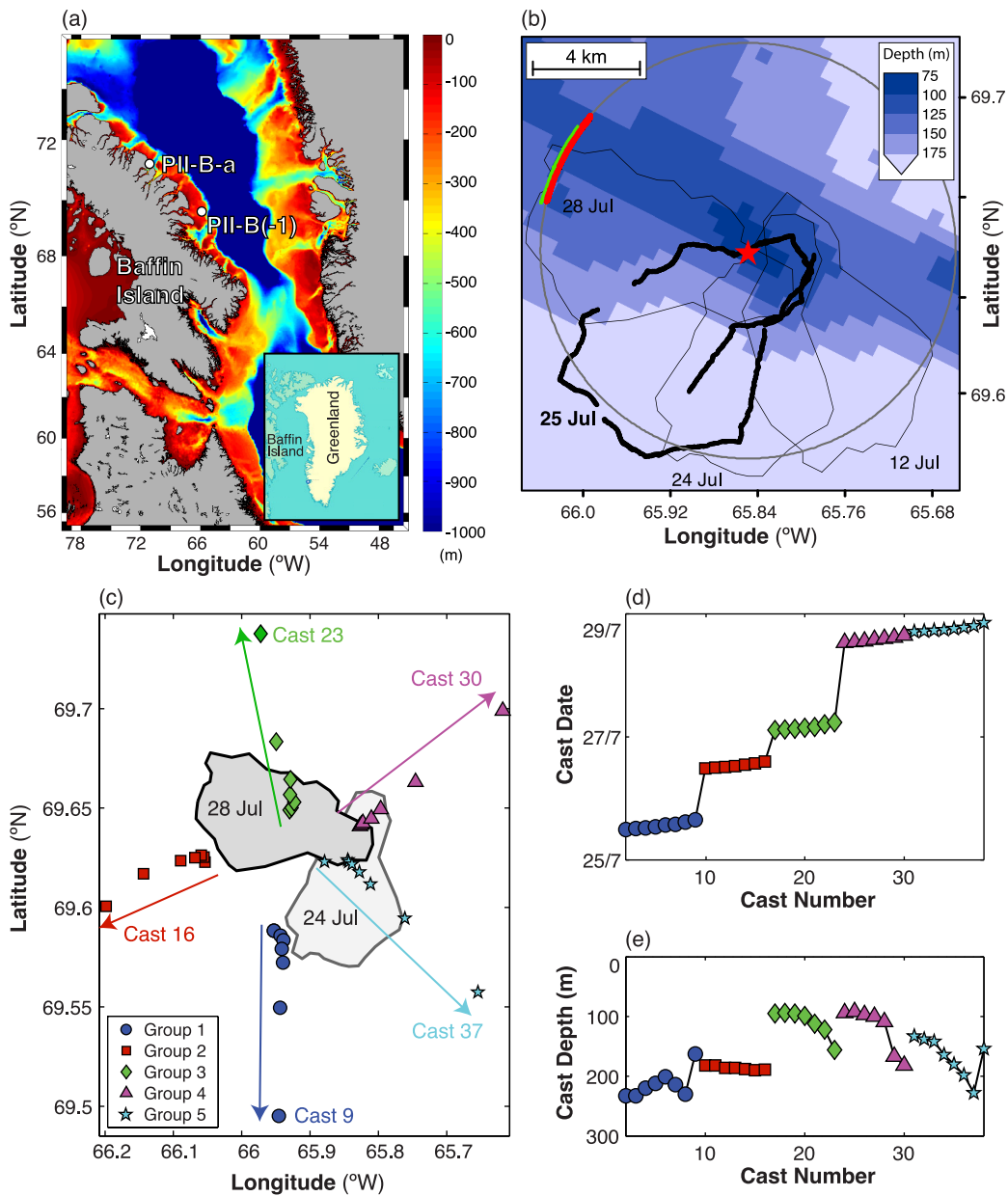


Figure 2. (a) Regional bathymetry in Baffin Bay taken from the ETOPO1 data set [Amante and Eakins, 2009]. The position of PII-B-1 and PII-B-a are shown. (b) Local bathymetry around PII-B-1, taken from IBCAO V3 [Jakobsson et al., 2012]. Red and green curves show the position of the GPS units which were deployed on PII-B-1. Outlines of the iceberg, traced from MODIS satellite images from 12, 24, and 28 July 2012, are shown with thin black lines. The thick black line is from the first lidar survey of the iceberg on 25 July 2012; the iceberg rotated during the survey, so the line is not closed. A circle is plotted around the point marked with a star, which is approximately the point where the iceberg was grounded. (c) Positions, (d) times, and (e) depths of CTD casts collected around PII-B-1 during the July 2012 survey. MODIS image traces of the iceberg from 24 and 28 July 2012 also are shown in Figure 2c.

Iceberg, and also published by Wagner et al. [2014]. At the time of the campaign, PII-B-1 had a surface area of $\sim 42 \text{ km}^2$.

During this second visit a more comprehensive CTD survey was performed around the iceberg, using an ADM mini CTD probe. The CTD survey was organized in 5 groups which began $< 1 \text{ km}$ from the iceberg edge and moved radially outwards to $\sim 10 \text{ km}$ from the iceberg edge, sampling at approximately logarithmic spacing. These five groups are referred to as Group 1 to Group 5 throughout this study. The location, time and ocean depth of each CTD cast are shown in Figures 2c–2e, respectively.

A Doppler current meter was used to make current measurements at three different depths (5, 50, and 100 m), using bottom tracking when in range. GPS location data were logged by the ship, as well as by GPS sensors located on the iceberg between 30 July and 3 August 2012 to monitor the iceberg motion. The iceberg side above the waterline was scanned with an Optec lidar, and the iceberg side beneath the waterline was mapped using a Reson SeaBat 8125 455 kHz multibeam sonar (see Wagner *et al.* [2014] for further details). The average thickness of the iceberg was ~ 70 m. The positions of the iceberg on 12, 24, and 28 July 2012 are shown in Figure 2b. These iceberg outlines were traced from images recorded by the Moderate Resolution Imaging Spectroradiometer (MODIS) sensor on the NASA Terra satellite.

One further CTD survey was performed on 10 August 2013 around PII-B-a, one of the aforementioned smaller fragments that calved from PII-B. On 10 August 2013, PII-B-a had a surface area of 8.4 km^2 (measured using RADARSAT-2 images), and was grounded at $71^\circ 20' \text{N}$, $71^\circ 02' \text{W}$ (Figure 2a). Measurements were made around PII-B-a using a moving vessel profiler (MVP), with an AML Micro CTD sensor attached. The MVP circled the iceberg, remaining 50–100 m from the iceberg edge, and performing 61 dives.

Information about the accuracy of instruments used in all three field campaigns are reported in supporting information Table S1. CTD data were processed using the TEOS-10 Oceanographic Toolbox [McDougall and Barker, 2011]. All conductivity measurements have been converted to absolute salinity (units of g/kg), and all densities are sigma-0. The results below focus on the measurements made around iceberg PII-B-1 in July 2012. Results from the 2011 and 2013 campaigns are presented in support of the main findings.

2.2. Integrated Fresh Water and Heat Content

In our analysis below, we make use of the integrated fresh water content and integrated heat content of a given cast, defined as

$$F = \int_h^0 [S_0 - S(z)] dz, \quad (1)$$

and

$$H = \int_h^0 [T(z) - T_0] dz, \quad (2)$$

respectively. Here $T_0 = -1.71^\circ \text{C}$ and $S_0 = 33.63 \text{ g/kg}$, are the minimum temperature and maximum salinity found across all casts in the July 2012 ocean survey. We use $h = -80 \text{ m}$ as the integration depth, chosen as the depth at which all casts are at least 10 m above the sea floor. At the depth $h = -80 \text{ m}$, the temperatures and salinities were approximately equal across all casts. The qualitative conclusions drawn from the behavior of F and H are not sensitive to the choice of h within the range $-85 \text{ m} < h < -35 \text{ m}$. Note that the upper limit is significantly more shallow than the average thickness of the iceberg ($\sim 70 \text{ m}$).

2.3. Diagnostic for Upwelling/Downwelling Wind Direction

We introduce the quantity $C(t, \phi)$ which indicates whether a particular wind direction is expected to cause upwelling or downwelling offshore of the iceberg. $C(t, \phi)$ is defined as

$$C(t, \phi) = \frac{1}{\Delta t} \int_{t-\Delta t}^t u(\phi + 90^\circ) dt \quad (3)$$

where

$$u(\phi) = \mathbf{u} \cdot \langle \cos \phi, \sin \phi \rangle \quad (4)$$

is the component of the wind in the direction ϕ , \mathbf{u} is the wind velocity vector, and ϕ is defined as the outward direction from the center of mass of the iceberg measured in degrees counterclockwise from due east. Since the Ekman transport in the northern hemisphere moves 90° clockwise of the wind direction, $u(\phi + 90^\circ)$ gives a measure of the amount of offshore Ekman transport we expect in a direction ϕ , for a given wind, \mathbf{u} . $C(t, \phi)$ is the time-average of $u(\phi + 90^\circ)$ over the period $\Delta t = 24 \text{ h}$ preceding time t , and therefore gives a measure of whether on average the wind has been in a direction consistent with upwelling (positive C) or downwelling (negative C) over the last 24 h.

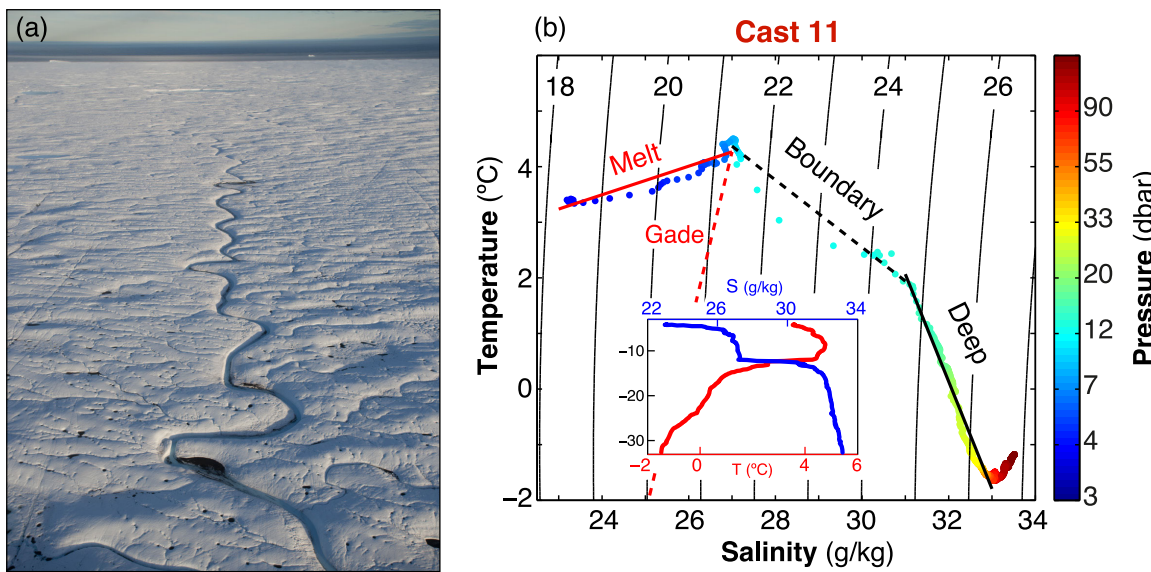


Figure 3. (a) Photograph of iceberg PII-B-1 taken from above. A meltwater channel can be seen on the surface of the iceberg. (b) T-S diagram for Cast 11, collected nearby to where the meltwater channel entered the ocean. The inset shows the temperature (red) and absolute salinity (blue) profiles of the cast. A “runoff mixing line” and Gade line are plotted on the T-S diagram (see section 3.2 for details).

3. Results

3.1. Rotation of PII-B-1 Around a Pivot Point

A time series of the location of the GPS deployed on PII-B-1 from 30 July to 3 August 2012 shows the iceberg moving back and forth across the arc shown in Figure 2b (the time series is not shown). Current data collected during this time show that the current is dominated by a barotropic diurnal tide. The motion of the on-ice GPS was almost perfectly in-phase with the tidal currents. Completing the circle from the arc of the GPS record reveals the approximate location of the pivot point, marked with a star on Figure 2b. This location corresponds to a topographic rise observed in the IBCAO V3 [Jakobsson et al., 2012] bathymetry data set, and is positioned close to the shallowest bathymetry observed using the ship’s sonar (92 m). MODIS images of the iceberg from 12 to 28 July 2012 are consistent with the iceberg rotating around the indicated pivot point (Figure 2b). From this we infer that one end of the iceberg was grounded on a shallow topographic rise, and the other end was rotating back and forth with the tides, creating the arc shown in Figure 2b. Between 12 and 28 July 2012, the iceberg rotated counterclockwise around the pivot point by $\sim 180^\circ$, presumably driven by wind and mean surface currents.

3.2. Melting and Meltwater

An estimate of the melt rates on the surface, sides, and base of PII-B-1 was calculated using energy balance arguments together with in situ ocean data, as well as atmospheric conditions taken from European Centre for Medium-Range Weather Forecasts (ECMWF) daily ERA-Interim reanalysis fields [Dee et al., 2011]. Details of this calculation and a discussion of possible sources of error are given in the supporting information. A time series of the volume of meltwater from the surface, sides, and base of PII-B-1 over a six month period from March to August 2012 is presented in supporting information Figure S2.

The melt rate estimates suggest that a relatively small amount of melting takes place at the base of the iceberg. This implies that upward motion due to buoyant meltwater production beneath the iceberg is likely to have a small effect on the surrounding ocean.

This result was partially confirmed using a neutrally buoyant colored dye, released by human divers along the sides of the iceberg at 18 m below the surface. The dye showed little evidence of upward motion, which indicated the absence of an upward buoyancy current along the sides of the iceberg. Video footage of the dye being released along the side of the iceberg is included in the supporting information.

The largest contribution to the melt rate was from the sides of the iceberg where warm surface waters and wave energy cause the formation of a “wavecut” near the waterline, leading to the collapse of the over-

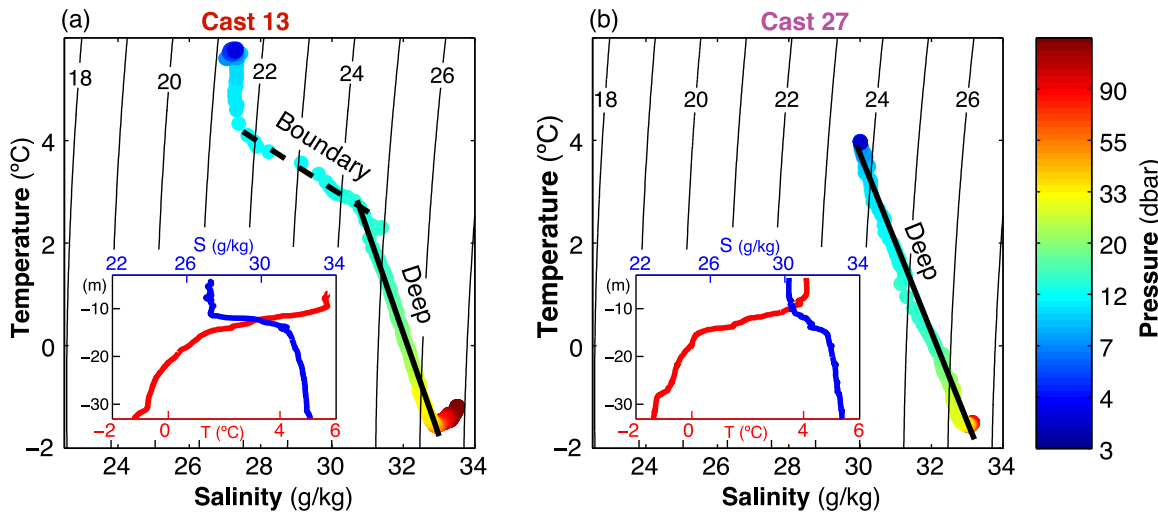


Figure 4. T-S diagram for (a) Cast 13 (Group 2) and (b) Cast 27 (Group 4), collected in July 2012 around PII-B-1. The colors of the plots indicate the pressure at which the measurements were made. The T-S diagrams in both plots have been fitted with straight lines which indicated the mixing lines (see section 4.1). The insets show the temperature (red) and absolute salinity (blue) profiles of the casts.

hanging ice. The erosion at the sides of the iceberg occurs almost exclusively above the thermocline since (a) the surface water is warmer than water at depth, and (b) surface waves cause increased turbulent exchange between the water and the iceberg. The erosion at the sides of the iceberg is greatly enhanced during summer when the sea ice clears, as the absence of sea ice allows the surface waters to warm and also allows increased wave motion [Bigg *et al.*, 1997]. The large amount of near-sea-level erosion at the sides of the iceberg suggests that the aforementioned footloose mechanism is likely a significant contributor to the decay of PII-B-1 [Wagner *et al.*, 2014].

Melting on the surface of the iceberg is the second largest contributor to the total melt. Rivers of surface runoff water were observed to flow into the ocean through large channels that develop on the iceberg surface (Figure 3a). The effect of this surface runoff on the surrounding ocean can be observed in the T-S diagram of Cast 11 (Figure 3b), which was collected near to where a meltwater river entered the ocean. As the runoff mixes into the ocean mixed layer, it causes the mixed layer to become stratified, as different proportions of meltwater mix in at different depths. This mixing process creates a “runoff mixing line” on the T-S diagram, which can be extended to the point $(T, S) = (T_f, 0)$. Here $T_f = 0^\circ\text{C}$ is the freezing point of fresh water. This “runoff mixing line” is notably distinct from the Gade line, which can be extended to the point $(T, S) = \sim (-L/c_p, 0)$ [Gade, 1979], indicating that the meltwater was not created by subsurface melting. Here L is the latent heat of fusion of ice, and c_p is the specific heat of water. Such “runoff mixing lines” were observed in just two of the 38 casts, suggesting that runoff mixes rapidly with the surrounding ocean. The temperature and salinity profiles of more typical casts (Figure 4) are discussed in the next section.

3.3. Ocean Conditions Around PII-B-1

CTD profiles collected around PII-B-1 from 25 to 29 July 2012 show substantial variations in the mixed layer temperatures and salinities at different locations around the iceberg. In general, surface water was observed to be $\sim 2^\circ$ warmer and ~ 3 g/kg fresher on the southern and western side of the iceberg than on the eastern side. Most of the temperature and salinity differences occurred in the top 30 m of the water column, while relatively little variation was observed further down. For example, the temperature and salinity profiles of Cast 13, collected on the northwestern side of the iceberg, and Cast 27, collected on the eastern side, are shown in the insets of Figures 4a and 4b, respectively. Cast 13 has a surface temperature $\sim 6^\circ\text{C}$ and salinity ~ 27 g/kg, while the surface temperature and salinity of Cast 27 are $\sim 4^\circ\text{C}$ and ~ 30 g/kg, respectively.

The asymmetries around the iceberg can be clearly seen when the casts are divided into the five groups, based on their orientation around the iceberg. Figures 5a–5e show temperature sections for the upper 30 m of the water column in Groups 1 to 5, respectively, with density contours overlain (the density is

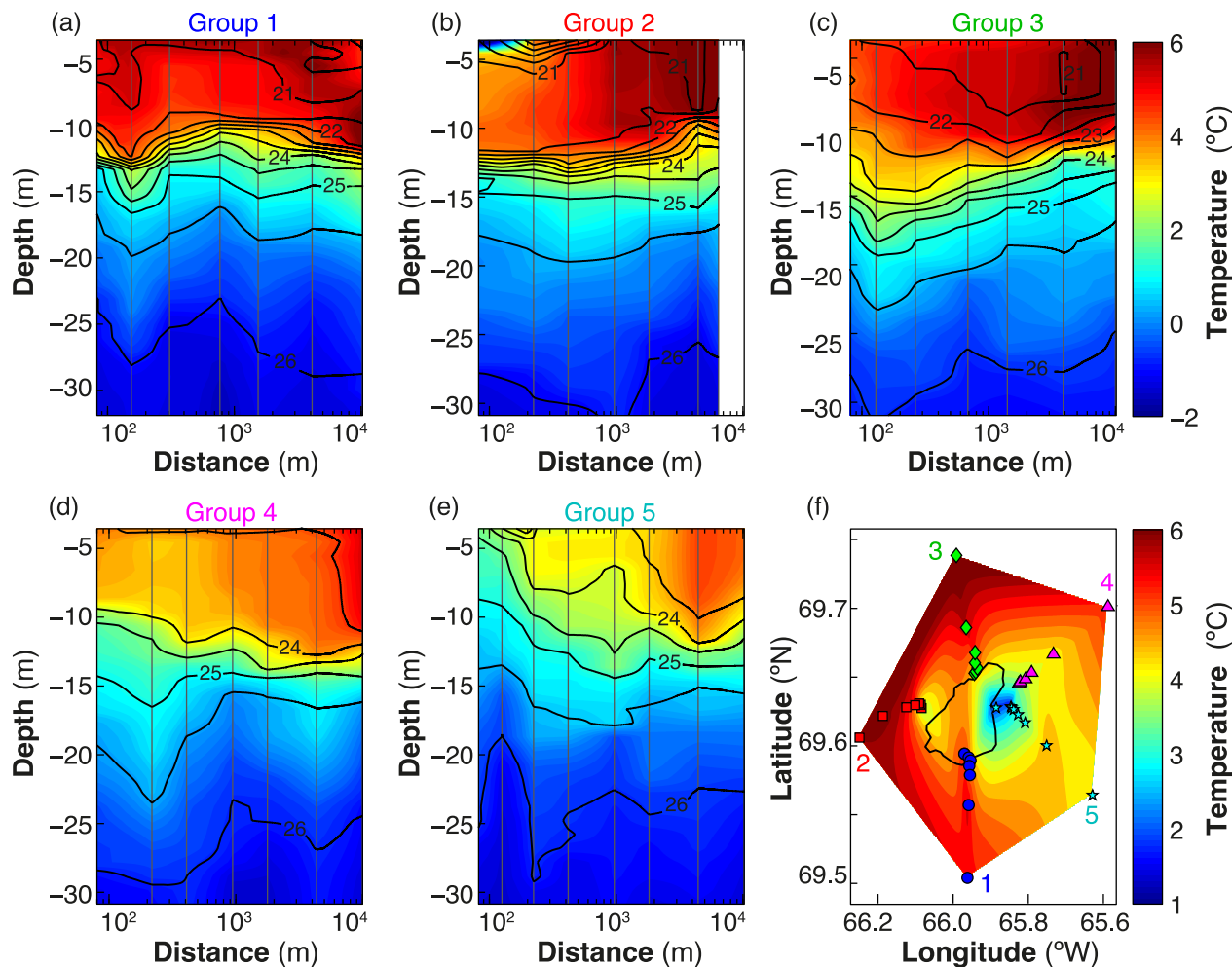


Figure 5. (a-e) The temperature sections around PII-B-1 collected in July 2012 in Group 1 to Group 5, respectively. The vertical axis shows depth below sea level, and the horizontal axis shows distance from the iceberg on a logarithmic scale. Density contours over overlaid. The position of each cast is shown by the vertical grey lines. (f) An interpolation of the ocean temperatures 5 m below the surface. The position of the casts in each group is shown by the colored symbols.

dominated by the effect of salinity). Figure 5f shows an interpolation of the ocean temperature 5 m below the surface. Figure 6 is analogous to Figure 5, giving the corresponding salinity profiles. Overall, the profiles show a warm fresh water layer in the upper ocean with a sharp transition to the cooler salty waters below. The upper ocean is warmest and freshest in Groups 1 and 2 (collected to the south and west of the iceberg, respectively), while temperatures are lower and salinities are higher in Groups 4 and 5 (collected to the northeast and southeast of the iceberg, respectively). The isopycnals at the base of the thermocline are mostly flat in Groups 1 and 2 (Figures 5a and 5b). In Groups 4 and 5, by contrast, these isopycnals are tilted upwards towards the iceberg (Figures 5d and 5e), suggesting the presence of upwelling on this side of the iceberg. Groups 1 and 2 have a sharp temperature and density transition at the base of the thermocline, while the transition in Groups 4 and 5 is more gradual. Group 3 (collected on the northern side of the iceberg) is an intermediate case which shares some properties with Group 1 and 2, and some with Groups 4 and 5, as discussed below.

Similar asymmetries in the upper ocean salinity and temperature to those of the 2012 data are observed in the data collected around PII-B in October 2011 and around PII-B-a in August 2013. Figures 7a, 7b, 8a, and 8b show the temperature and salinity sections around PII-B and PII-B-a, with density contours overlaid. The path of the ship and locations of the CTD profiles around PII-B and PII-B-a are shown in Figures 7c and 8c, respectively. Figures 7a and 7b show the presence of warmer and fresher water to the west of PII-B, and cooler, more saline water to the east. The deepening of the base of the thermocline on the western side of

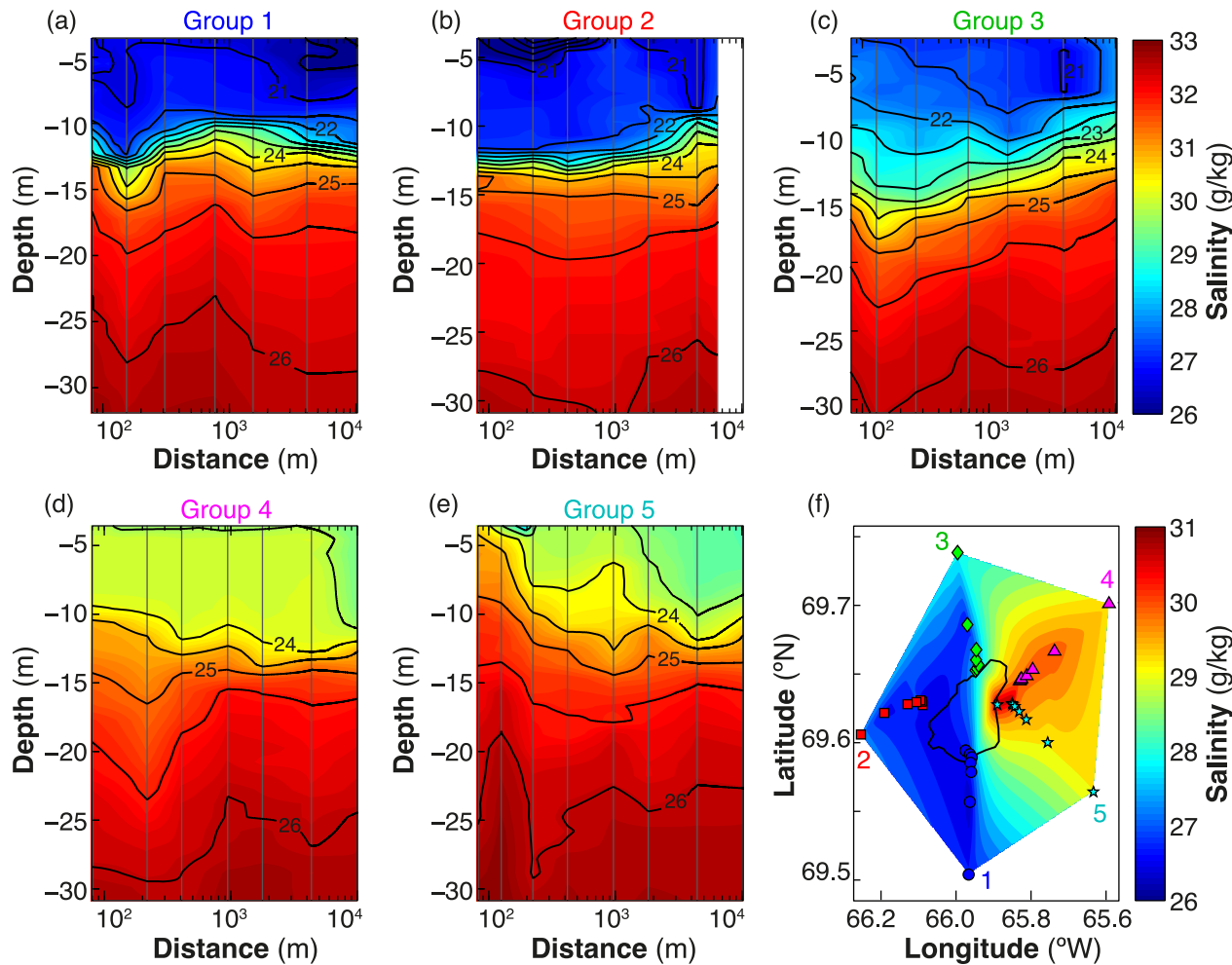


Figure 6. As for Figure 5, but with absolute salinity instead of temperature.

the iceberg suggests the presence of downwelling in this region. Figures 8a and 8b show anomalously cool and saline water on the western side of PII-B-a, compared to the warmer fresher water on the eastern side. The shoaling of the base of the thermocline to the west of PII-B-a suggests the presence of upwelling in this region.

4. Discussion

We propose the following mechanism to explain the observed asymmetries in temperature and salinity in the upper ocean around the icebergs (see schematic in Figure 1): surface winds give rise to a surface Ekman transport in the upper ocean. On one side of the iceberg, this Ekman transport moves surface water away from the iceberg, causing upwelling which cools the upper ocean. On the opposing side of the iceberg, the Ekman transport causes the surface water to pile up against the iceberg, causing enhanced stratification and warming of the upper ocean. The resultant asymmetries in upper ocean temperatures cause increased iceberg decay on the warmer side of the iceberg through enhanced melting, as well as through the foot-loose mechanism.

4.1. Vertical Mixing Around PII-B-1

Insight into the extent of vertical mixing around PII-B-1 can be gained by considering the mixing lines in the T-S diagrams around the iceberg. Figure 4a (Cast 13 in Group 2) has two visible mixing lines, indicating that there is vertical mixing above and below the base of the thermocline, but little vertical mixing between the water at depth and the water in the thermocline. The fact that the upper ocean

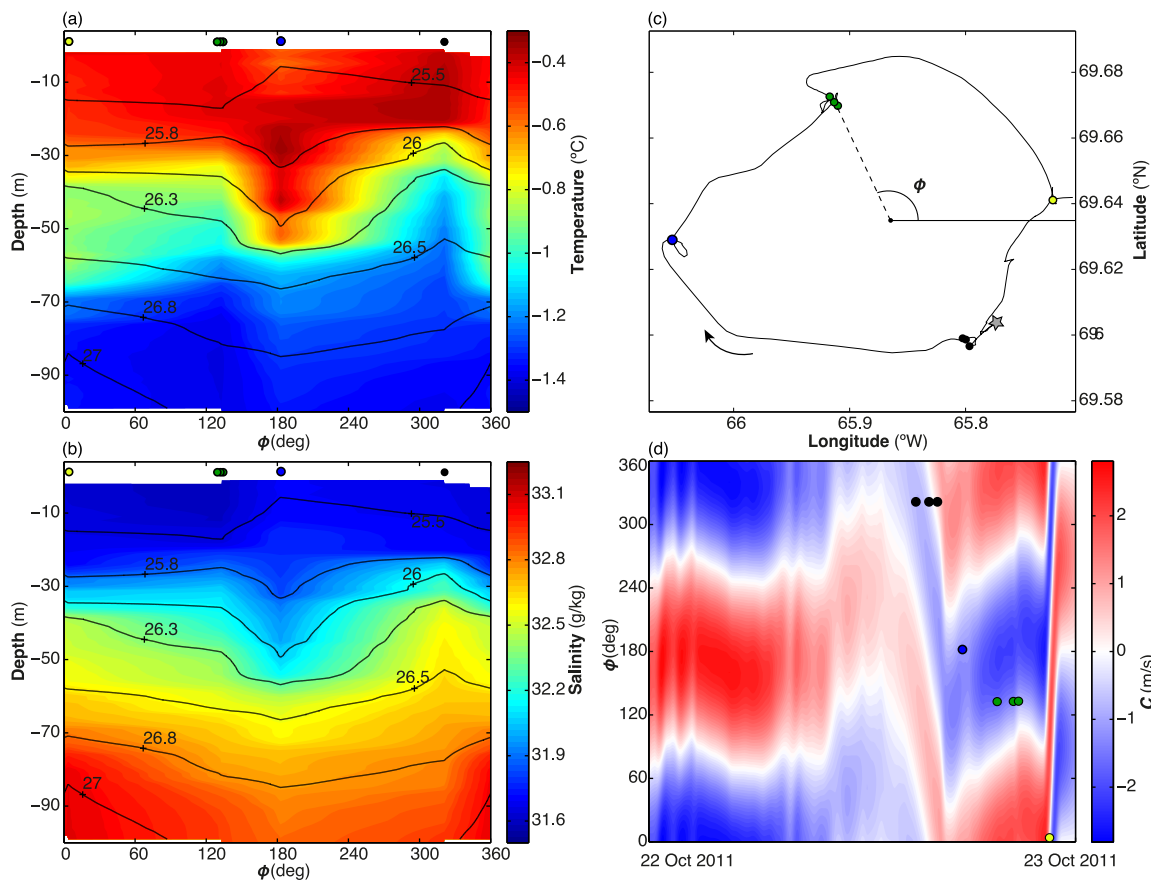


Figure 7. (a) Temperature and (b) absolute salinity sections around PII-B, collected in October 2011, with density contours overlain. (c) The position of CTD casts and the ship's route around the iceberg. The ship's starting position is indicated by a star, and the direction of motion is indicated by an arrow. (d) Hovmöller diagram of the quantity $C(\phi, t)$. The position of each cast is plotted on the Hovmöller diagram. A blue dot has been used to indicate the locations and times of the downwelling cast in all four plots.

temperatures and salinities do not lie on the “deep mixing line” implies that this water is affected by nonconservative surface processes [Jenkins, 1999]. In Cast 13, the upper ocean is likely influenced by insolation and by mixing with meltwater runoff, both of which reduce the density of the water in the thermocline. The two separate mixing lines of Cast 13 are typical of the casts in Groups 1 and 2, and suggest that warmer fresher water is trapped near the surface in these two groups. In contrast, Figure 4b (Cast 27 in Group 4) has just one mixing line indicating that water from below the thermocline is able to mix conservatively with water at the surface. This suggests that for Cast 27, any water affected by non-conservative surface processes must be continuously transported away by surface currents. Since the amount of insolation and meltwater runoff is unlikely to depend on the orientation around the iceberg, this suggests that the surface water in Cast 27 has been advected away by surface currents, and replaced by upwelling water from below. The single mixing line on the T-S diagram of Cast 27 is similar to all casts in Groups 4 and 5, suggesting that the colder, more saline water found in the mixed layer in these two groups, has upwelled.

4.2. Evidence of an Overturning Circulation

Figure 9a shows how the integrated freshwater content, F (defined in section 2.2), varies with distance from the iceberg for each cast. The freshwater content is consistently larger in Groups 1 and 2 than in Groups 4 and 5. Since F is a vertically integrated quantity, this implies that the asymmetries observed around the iceberg are not formed by vertical mixing alone, but rather require some horizontal advection to supply or remove fresh water from the water column. F decreases with distance to the iceberg in Group 2 and remains broadly constant in Group 1. In Groups 4 and 5, by contrast, F increases with distance from the iceberg.

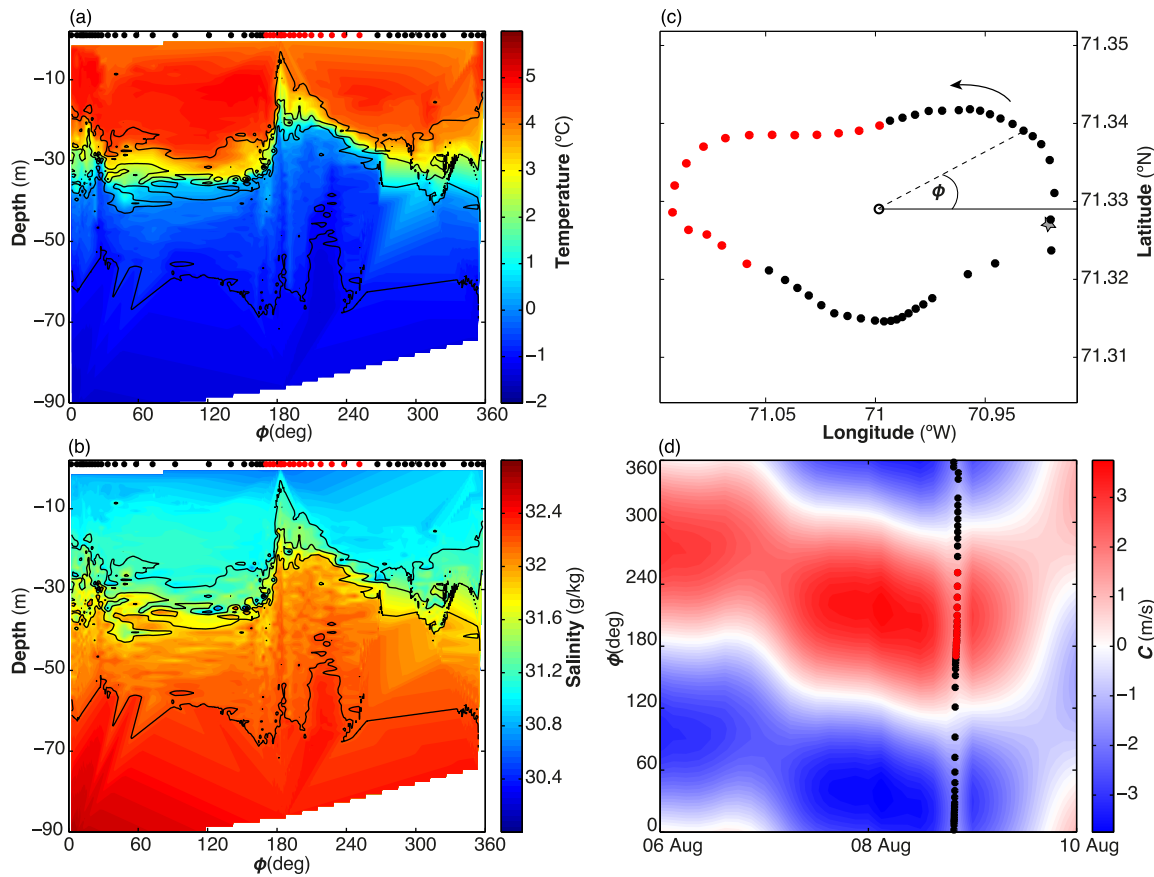


Figure 8. As for Figure 7, but for measurements around iceberg PII-B-a in August 2013. Figure 8d is created using the ERA-Interim reanalysis wind data at 10 m above the surface, and has a 3 h time resolution. The density contours in Figures 8a and 8b are in the range 23.9–26.2 kg/m³.

Similarly, Figure 9b shows that the integrated heat content of the water column, H , mostly increases with distance from the iceberg in Groups 4 and 5, while the behavior is less clear in Groups 1 and 2. F and H are positively correlated with one another with a correlation of $r=0.785$ (Figure 9d). The fact that the coolest, most saline water is found close to the iceberg in Groups 4 and 5, suggests that the upwelling is strongest close to the iceberg, and decreases in strength with increasing radial distance. This suggests the presence of an overturning cell on the eastern side of the iceberg: cool dense water is advected towards the iceberg at depth, when it reaches the iceberg it upwells to the surface, and it is then transported away from the iceberg by surface currents. This causes the isopycnals in Group 4 and 5 to slant upwards (Figures 5d and 5e), F and H to be smallest close to the iceberg (Figure 9), and the mixing lines on the corresponding T-S diagrams to extend to the surface (Figure 4a). Conversely, the results for Groups 1 and 2 suggest that warm fresh water is advected towards the iceberg at the surface. Since the surface water is much less dense than the water below the thermocline, it does not mix easily with the water below it. This causes the warm surface water in Groups 1 and 2 to pile up against the iceberg, and results in the large values of F and H that are found there. It further leads to large maximum density gradients, $(d\rho/dz)_{max}$, at the base of the thermocline, compared with consistently smaller values in Groups 4 and 5 (Figure 9c).

As mentioned before, Group 3 is an intermediate group that shares certain properties with Groups 1 and 2, and other properties with Groups 4 and 5. The upper ocean in Group 3 is relatively warm and fresh, and is similar to that of Groups 1 and 2. This results in large values for the integrated fresh water content, F , and integrated heat content, H , in Group 3. However, the density gradients at the base of the thermocline in Group 3 are not as sharp as in Groups 1 and 2, and some of the isopycnals slope upwards towards the iceberg, as in Groups 4 and 5. A possible explanation is that Group 3 is in a transitional state, changing from enhanced stratification (as in Groups 1 and 2) to ocean upwelling (as in Groups 4 and 5).

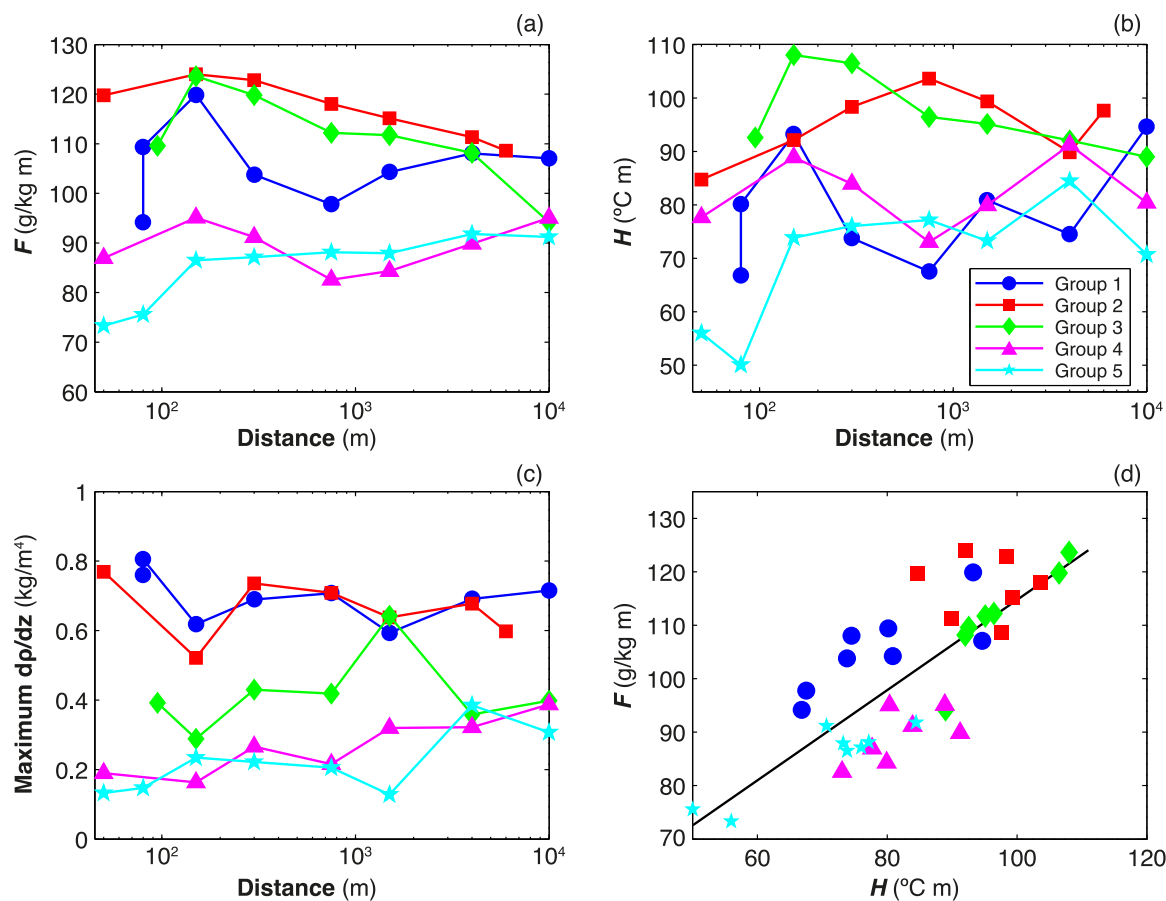


Figure 9. (a-c) How properties of the water column change with distance from PII-B-1 in July 2012 are shown: (a) vertically integrated freshwater content, (b) vertically integrated heat content, (c) maximum vertical density gradient in the water column. (d) The relationship between freshwater content and heat content for the different casts.

4.3. Wind-Driven Upwelling and Enhanced Stratification

Based on these findings, we propose that the observed asymmetries around PII-B-1 were caused by wind-driven upwelling and wind-driven enhanced stratification of the thermocline, occurring on opposite sides of the iceberg. This observed upwelling is analogous to wind-driven coastal upwelling. The grounded iceberg acts in place of the land mass, and allows upwelling to occur when the offshore direction is to the right of the prevailing wind direction. To the left of the wind, the surface water is driven towards the iceberg. Since the surface water is much less dense than the water below, the surface water does not mix easily with the water below it, and warm fresh water piles up against the iceberg causing a sharpening of the density gradients at the base of the thermocline (see schematic in Figure 1).

To test whether the mechanism is consistent with the observed asymmetries, we consider ERA-Interim reanalysis wind data for the 2012 observation period, since no wind data were collected in situ. Figures 10b and 10c show the wind direction and wind speed, respectively, at the location of the iceberg from 25 to 30 July 2012. Figure 10a is a Hovmöller diagram of the quantity $C(t, \phi)$, defined in section 2.3. Positive values of $C(t, \phi)$ imply winds with upwelling in the offshore direction ϕ , negative values of $C(t, \phi)$ imply winds with downwelling or enhanced stratification in the offshore direction ϕ . The position and time of the CTD casts are also shown in Figure 10a. Figure 10a shows that the CTD casts in Groups 1 and 2 were collected after a period where the wind was consistent with downwelling (causing a sharpening of the thermocline), and casts in Groups 4 and 5 were collected after a period where the wind was consistent with upwelling. Group 3's casts were collected after a short period of weak upwelling winds; however, we also observe that the wind direction had changed from downwelling winds to upwelling winds approximately one day before the casts were collected. These results therefore support the upwelling/enhanced stratification mechanism described above.

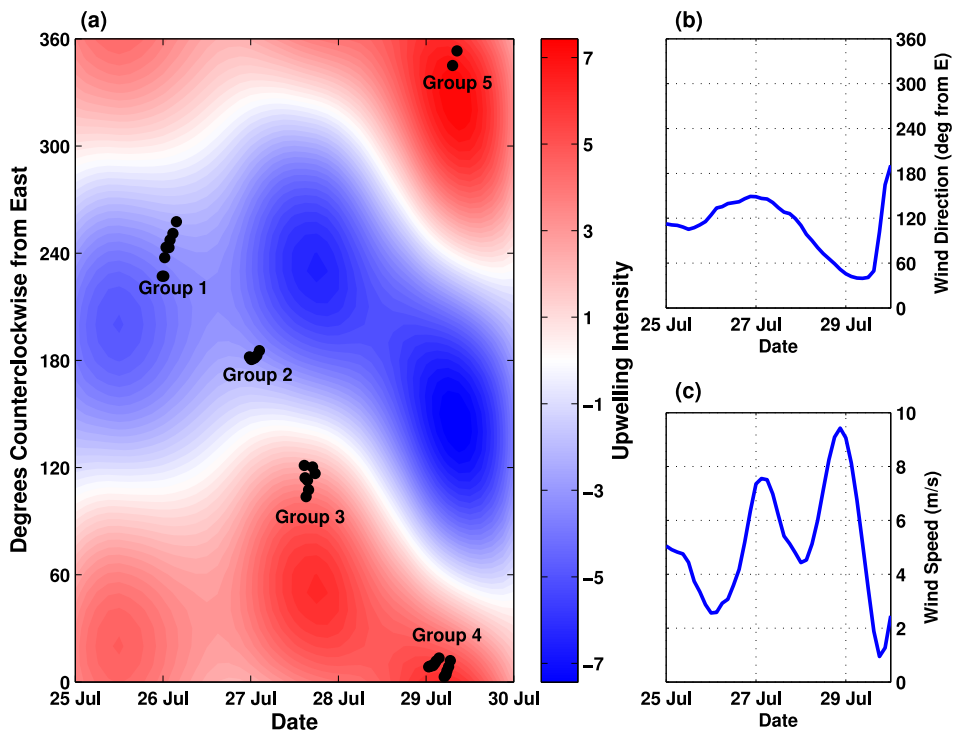


Figure 10. (a) Hovmöller diagram of the quantity $C(\phi, t)$, where ϕ is the angle of rotation counterclockwise from due east. The location/time of each cast is plotted on the Hovmöller diagram. The (b) wind direction and (c) wind speed are shown. The wind data are from the ERA-Interim reanalysis product and have a 3 h time resolution.

Figures 7d and 8d show Hovmöller diagrams of $C(t, \phi)$, for the wind around iceberg PII-B in October 2011, and PII-B-a in August 2013, respectively. Figure 7d is computed from wind data collected in situ (see section 2.2), while Figure 8d again uses ERA-Interim reanalysis wind data. Figure 7d shows that the deepening of the thermocline on the west of the iceberg (blue dot) occurs after a period of wind consistent with downwelling on that side of the iceberg. In Figure 8d, we observe that the shoaling of the base of the thermocline to the west of PII-B-a (red dots in Figure 8) occurs after winds consistent with upwelling on that side of the iceberg.

A number of other physical processes may contribute to variations in temperature and salinity fields, including tidal effects, subsurface melt, buoyancy forces and the observed diurnal iceberg rotation. However, none of these were found to have a notable impact on the water column (see supporting information for a discussion of the listed processes).

4.4. Differential Iceberg Deterioration

In the previous sections, we argued that wind-induced upwelling and enhanced stratification on opposing sides of a grounded iceberg can result in large asymmetries in surface temperatures around the iceberg. This suggests that the predominant wind patterns may indirectly play a central role in the degradation of the iceberg. In particular, on the side of the iceberg where the stratification at the base of the thermocline is enhanced, warmer thermocline temperatures would lead to increased iceberg melt near sea level, and as a knock-on effect, to expedited decay through the footloose mechanism.

To test this idea, we consider the degradation of PII-B-1 from 8 January 2012 through 1 August 2012. The iceberg's perimeter was digitized from four successive RADARSAT-2 Fine-Quad (8 m resolution) images, acquired during this period. Since the iceberg was pivoting on its grounding point, the shapefiles were manually corrected for rotation.

Figure 11a shows digitized outlines of the iceberg on 8 January (green), 28 February (pink), 14 June (blue), and 1 August 2012 (white), stacked chronologically. In this figure, we see that most of the iceberg deterioration occurred on the “southern” side of the iceberg. To quantify this preferential deterioration more

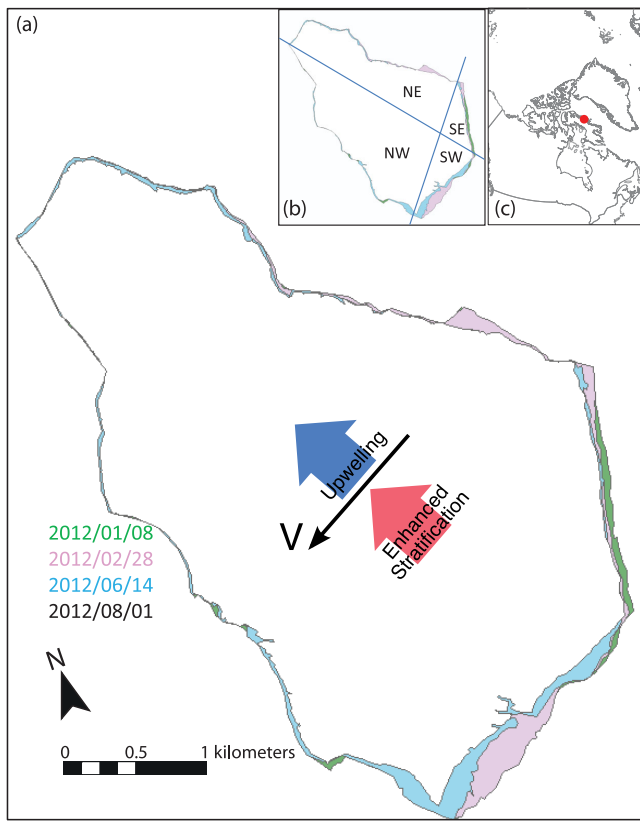


Figure 11. (a) Areal deterioration of PII-B-1 during 2012 as determined through digitization of RADARSAT-2 Fine-Quad imagery. The arrow labeled V show the time-average wind direction during the sea-ice free part RADARSAT-2 monitoring period. The red and blue arrows show the direction of the Ekman transport consistent with the wind direction V . (b) Quadrants used for preferential deterioration assessment. (c) The location of PII-B-1 marked by the red dot.

surface waters in this direction. This is broadly consistent with a greater deterioration rate on the southern side of the iceberg. The time-averaged wind direction at the location of PII-B-1 from July 4th (when the sea ice began to clear) to the end of the RADARSAT-2 monitoring period, when most of the surface melting is likely to occur, was in the direction $\theta=210^\circ$. This wind direction, shown with an arrow marked V on Figure 11, implies maximum stratification in the direction $\phi=300^\circ$, in agreement with increased decay on the southwest quadrant of the iceberg.

5. Conclusion

Hydrographic data collected around two grounded icebergs in Baffin Bay during three field campaigns show asymmetries in the ocean temperature and salinity around the icebergs. Regions of warm, fresh surface water are observed on one side of the iceberg, while the opposite side is cooler and saltier. An analysis of the data indicates that these asymmetries are likely to be caused by wind-induced ocean upwelling and wind-induced enhanced stratification, occurring on opposite sides of the iceberg. Wind-induced upwelling causes the mixed layer to be cooler and more saline on one side of the iceberg, while on the opposite side, a sharpening of the density gradients at the base of the thermocline causes the mixed layer to be warmer and fresher. Wind data, taken from ERA-Interim reanalysis and in situ measurements, are found to support this mechanism.

It is hypothesized that these asymmetries in ocean temperature lead to preferential deterioration on one side of the iceberg through enhanced melting, as well as through the iceberg footloose mechanism [Wagner et al., 2014]. This suggests that wind direction and speed can significantly influence the rate of degradation around a grounded iceberg. The theory was tested by monitoring the decay of PII-B-1 using satellite

precisely, we divide the iceberg into four quadrants, as shown in Figure 11b, and calculate the areal difference between the first (8 January) and last (1 August) iceberg outline for each quadrant. PII-B-1 experienced 1.8 km^2 of deterioration over the 7.5 months of RADARSAT-2 monitoring. The southwest and southeast quadrants accounted for the majority of PII-B-1's decrease in surface area with 0.47 km^2 and 0.88 km^2 lost over each, respectively. The combined areal deterioration of the southern quadrants represented 75 percent of the iceberg's total decrease in surface area, while only 27 percent of the iceberg's perimeter was located within these two quadrants.

The wind direction from ERA-Interim reanalysis surface data at the location of PII-B-1, averaged over the entire RADARSAT-2 monitoring period (including the period when the ocean was covered by sea ice) was in the direction $\theta=157^\circ$, where θ is measured counterclockwise from east. This wind direction implies maximum downwelling (or enhanced stratification at the base of the thermocline) in the direction $\phi=247^\circ$ counterclockwise from east, which would result in warmest

imagery and comparing the results with reanalysis wind data. The iceberg was observed to decay preferentially on one side, with the location of enhanced decay and time-averaged wind direction being consistent with the theory. This wind-induced upwelling and asymmetric iceberg decay, observed here around grounded tabular icebergs, may also be relevant to free-drifting icebergs, although in that context the effects may be more difficult to isolate and observe.

Acknowledgments

Special thank you to the BBC crew on Operation Iceberg, and the crew of *MV Neptune*. Information about the television documentary Operation Iceberg can be found at <http://www.bbc.co.uk/programmes/p00tvcnx>. Thanks to Chris Packham who took the photo in Figure 2a, and to Sarah Conner for help with editing the dye experiment clip. Funding for this project was also provided by NYU Abu Dhabi Research Institute for support under grant G1204 and NSF Polar Programs for support under grant ARC-1304137. We would like to acknowledge the following organizations and individuals for the additional data: the Canadian Ice Service (Environment Canada; specifically Leah Braithwaite), ArcticNet, and the captain and crew of CCGS *Amundsen*; Derek Mueller (Carleton U.) and the other members of the 2011 CCGS *Amundsen* iceberg campaign, Alexander Forrest (U. California Davis-Tahoe), Andrew Hamilton (U. British Columbia), Bernard Laval (U. British Columbia) and Richard Yeo (AUV Consultants). Also, thanks to Yves Gratton (From INRS-ETE, Quebec City, Canada) and Pascal Guillot (ISMER-UQAR, Rimouski, Canada) for the quality control of the CTD data. CTD data have been uploaded to the NCEI data center and is available under the reference ID J9YRT7.

References

- Amante, C., and B. W. Eakins (2009), *ETOPO1 1 arc-minute global relief model: procedures, data sources and analysis*, US Department of Commerce, National Oceanic and Atmospheric Administration, National Environmental Satellite, Data, and Information Service, Nat. Geophys. Data Cent., Marine Geology and Geophysics Division.
- Bakun, A. (1990), Global climate change and intensification of coastal ocean upwelling, *Science*, 247, 198–201.
- Biddle, L. C., J. Kaiser, K. J. Heywood, A. F. Thompson and A. Jenkins (2015), Ocean glider observations of iceberg-enhanced biological productivity in the northwestern Weddell Sea, *Geophys. Res. Lett.*, 42, 459–465, doi:10.1002/2014GL062850.
- Bigg, G. R., M. R. Wadley, D. P. Stevens, and J. A. Johnson (1997), Modeling the dynamics and thermodynamics of icebergs, *Cold Reg. Sci. Technol.*, 26, 113–135.
- Botsford, L. W., C. A. Lawrence, E. P., Dever, A. Hastings, and J. Largier (2003), Wind strength and biological productivity in upwelling systems: An idealized study, *Fish. Oceanogr.*, 12, 245–259.
- Botsford, L. W., C. A. Lawrence, E. P., Dever, A. Hastings and J. Largier (2006), Effects of variable winds on biological productivity on continental shelves in coastal upwelling systems, *Deep Sea Res., Part II*, 53, 3116–3140.
- Coogee, R. A., and A. M. Howard (2013), The iceberg observation problem: Using multiple agents to monitor and observe ablating target sources, in *2013 IEEE International Conference Systems, Man, and Cybernetics (SMC)*, pp. 1660–1665, IEEE, doi:10.1109/SMC.2013.286.
- Dee, D. P., et al. (2011), The ERA-Interim reanalysis: Configuration and performance of the data assimilation system, *Q. J. R. Meteorol. Soc.*, 137, 553–597.
- De Szoete, R. A. and J. G. Richman (1981), The role of wind-generated mixing in coastal upwelling, *J. Phys. Oceanogr.*, 11, 1534–1547.
- Dietrich, D. E., M. J. Bowman, C. A. Lin, and A. Mestas-Nunez (1996), Numerical studies of small island wakes in the ocean, *Geophys. Astrophys. Fluid Dyn.*, 83, 195–231.
- Dinniman, M. S., J. M. Klinck, and W. O. Smith Jr. (2007), Influence of sea ice cover and icebergs on circulation and water mass formation in a numerical circulation model of the Ross Sea, Antarctica, *J. Geophys. Res.*, 112, C11013, doi:10.1029/2006JC004036.
- Donaldson, P. B. (1978), Melting of Antarctic icebergs, *Nature* 275, 305306.
- Ekman, W. K. (1905), On the influence of Earth's rotation on ocean currents. *Ark. Mat. Astron. Fys.*, 2, 1–53.
- Falkner, K. K., et al. (2011), Context for the recent massive Petermann Glacier calving event, *Eos Trans. AGU*, 92, 117.
- Gade, H. G. (1979), Melting of ice in sea water: A primitive model with application to the Antarctic ice shelf and icebergs. *J. Phys. Oceanogr.*, 9, 189–198.
- Garvine, R. W. (1971), A simple model of coastal upwelling dynamics, *J. Phys. Oceanogr.*, 1, 169–179.
- Gladstone, R. M., G. R. Bigg, and K. W. Nicholls (2001), Iceberg trajectory modeling and meltwater injection in the Southern Ocean, *J. Geophys. Res.*, 106, 19,903–19,915.
- Grosfeld, K., M. Schröder, E. Fahrbach, R. Gerdes, and A. Mackensen (2001), How iceberg calving and grounding change the circulation and hydrography in the Filchner Ice Shelf Ocean System, *J. Geophys. Res.*, 106, 9039–9055.
- Halliday, E. J., T. King, P. Bobby, L. Copland, and D. Mueller (2012), Petermann Ice Island a survey results offshore labrador, paper presented at OTC Arctic Technology Conference, doi:10.4043/23714-MS.
- Helly, J. J., R. S. Kaufmann, G. R. Stephenson Jr., and M. Vernet (2011), Cooling, dilution and mixing of ocean water by free-drifting icebergs in the Weddell Sea, *Deep Sea Res., Part II*, 58(11–12), 1346–1363.
- Hossain, K., and A. R. Rao (2014), Environmental change and its affect, *Eur. J. Sustainable Dev.*, 3, 89–96.
- Hunkin, E. C., and D. Comeau (2011), Sea ice and iceberg dynamic interaction, *J. Geophys. Res.*, 116, C05008, doi:10.1029/2010JC006588.
- Huppert, H. E., and J. S. Turner (1980), Ice blocks melting into a salinity gradient, *J. Fluid Mech.* 100, 367–384.
- Hutchins, D. A., and K. W. Bruland (1998), Iron-limited diatom growth and Si: N uptake ratios in a coastal upwelling regime, *Nature*, 393, 561–564.
- Jakobsson, M., et al. (2012), The International Bathymetric Chart of the Arctic Ocean (IBCAO) Version 3.0, *Geophys. Res. Lett.*, 393, L12609, doi:10.1029/2012GL052219.
- Jenkins, A. (1999), The impact of melting ice on ocean waters, *J. Phys. Oceanogr.*, 29(9), 2370–2381.
- Jongma, J. I., E. Driesschaert, T. Fichefet, H. Goosse, and H. Renssen (2009), The effect of dynamic-thermodynamic icebergs on the Southern Ocean climate in a three-dimensional model, *Ocean Model.*, 26, 104–113.
- Kämpf, J., M. Doubell, D. Griffin, R. L. Matthews, and T. M. Ward (2004), Evidence of a large seasonal coastal upwelling system along the southern shelf of Australia, *Geophys. Res. Lett.*, 31, L09310, doi:10.1029/2003GL019221.
- Kaufmann, R. S., B. H. Robison, R. E. Sherlock, K. R. Reisenbichler, and K. J. Osborn (2011), Composition and structure of macrozooplankton and microneuston communities in the vicinity of free-drifting Antarctic icebergs, *Deep Sea Res., Part II*, 58(11–12), 1469–1484.
- Keghouche, I., L. Bertino, and K. A. Lister (2009), Parameterization of an Iceberg Drift Model in the Barents Sea, *J. Atmos. Oceanic Technol.*, 26, 2216–2227.
- Kubat, I., M. Sayed, S. B. Savage, T. Carrières, and G. Crocker (2007), An operational iceberg deterioration model, *Proceedings of the seventeenth international offshore and polar engineering conference*, Lisbon, Portugal, July 1–6, The International Society of Offshore and Polar Engineers, 652–657, Cupertino, Calif.
- Kusahara, K., H. Hasumi, and G. D. Williams (2011), Impact of the Mertz Glacier Tongue calving on dense water formation and export, *Nat. Commun.*, 2, 159.
- Martin, S., R. Drucker, R. Aster, and F. Davey (2010), Kinematic and seismic analysis of giant tabular iceberg breakup at Cape Adare, Antarctica, *J. Geophys. Res.*, 115, B06311, doi:10.1029/2009JB006700.
- Martin, T., and A. Adcroft (2010), Parameterizing the fresh-water flux from land ice to ocean with interactive icebergs in a coupled climate model, *Ocean Model.*, 34, 111–124.
- McDougall, T. J., and P. M. Barker (2011), *Getting Started With TEOS-10 and the Gibbs Seawater (GSW) Oceanographic Toolbox*, 28 pp., SCOR/IAPSO WG127. [Available at: <http://www.teos-10.org/software.htm>.]
- Neshyba, S. (1977), Upwelling by icebergs, *Nature*, 507–508.

- Nøst, O. A., and S. Østerhus (1998), Impact of grounded icebergs on the hydrographic conditions near the Filchner Ice Shelf, in *Ocean, Ice, and Atmosphere: Interactions at the Antarctic Continental Margin*, edited by S. S. Jacobs and R. F. Weiss, pp. 267–284, AGU, Washington, D. C.
- Peterson, I. K., J. S. Holladay, and L. Lalumiere (2012), Ocean and Ecosystem Sciences Division Maritimes Region Fisheries and Oceans Canada Bedford Institute of Oceanography, Dartmouth, Nova Scotia, Canada.
- Price, J. F., R. A. Weller, and R. R. Schudlich (1987), Wind-driven ocean currents and Ekman transport, *Science*, 238, 1534–1538.
- Robinson, N. J., and M. J. M. Williams (2012), Iceberg-induced changes to polynya operation and regional oceanography in the southern Ross Sea, Antarctica, from in situ observations, *Antarct. Sci.*, 24, 514–526, doi:10.1017/S0954102012000296.
- Robinson, N. J., M. J. M. Williams, P. J. Barrett, and A. R. Pyne (2010), Observations of flow and ice-ocean interaction beneath the McMurdo Ice Shelf, Antarctica, *J. Geophys. Res.*, 115, C03025, doi:10.1029/2008JC005255.
- Savage, S. B. (2001), Aspects of iceberg deterioration and drift, in *Geomorphological Fluid Mechanics, Lect. Notes Phys. Ser.*, vol. 582, edited by N. J. Balmforth, and A. Provenzale, pp. 279–318, Springer, Berlin.
- Scambos, T., O. Sergienko, A. Sargent, D. MacAyeal, and J. Fastook (2005), ICESat profiles of tabular iceberg margins and iceberg breakup at low latitudes, *Geophys. Res. Lett.*, 32, L23S09, doi:10.1029/2005GL023802.
- Send, U., R. C. Beardsley, and C. D. Winant (1987), Relaxation from upwelling in the coastal ocean dynamics experiment, *J. Geophys. Res.*, 92, 1683–1698.
- Shaw, T. J., R. Raiswell, C. R. Hexel, H. P. Vu, W. S. Moore, R. Dudgeon, and K. L. Smith Jr. (2011), Input, composition, and potential impact of terrigenous material from free-drifting icebergs in the Weddell Sea, *Deep Sea Res., Part II*, 58(11–12), 1376–1383.
- Silva, T. A. M., G. R. Bigg, and K. W. Nicholls (2006), Contribution of giant icebergs to the Southern Ocean freshwater flux, *J. Geophys. Res.*, 111, C03004, doi:10.1029/2004JC002843.
- Smith, K. B., R. Robison, J. Helly, R. Kaufmann, H. Ruhl, H. T. Shaw, and M. Vernet (2007), Free-drifting icebergs: Hotspots of chemical and biological enrichment in the Weddell Sea, *Science*, 317, 478–482.
- Smith, K. L., Jr. (2011), Free-drifting icebergs in the Southern Ocean: An overview, *Deep Sea Res., Part II*, 58(11–12):1277–1284.
- Smith, L. C., and S. R. Stephenson (2013), New Trans-Arctic shipping routes navigable by midcentury, *Proc. Nat. Acad. Sci. U. S. A.*, 110, E1191–E1195.
- Stephenson, G. R., Jr., J. Sprintall, S. T. Gille, M. Vernet, J. J. Helly and R. S. Kaufmann (2011), Subsurface melting of a free-floating Antarctic iceberg, *Deep Sea Res., Part II*, 58(11–12), 1336–1345.
- Takahashi, M., I. Koike, T. Ishimaru, T. Saino, K. Furuya, Y. Fujita, A. Hattori, and S.E. Ichimura (1980), Upwelling plumes in Sagami Bay and adjacent water around the Izu Islands, *Japan. J. Oceanogr. Soc. Jpn.*, 36, 209–216.
- Turnbull, I. D., N. Fournier, M. Stolwijk, T. Fosnaes, and D. McGonigal (2015), Operational iceberg drift forecasting in Northwest Greenland, *Cold Reg. Sci. Technol.*, 110, 1–18.
- Vernet, M., K. Sines, D. Chakos, A. O. Cefarelli, and L. Eker (2011), Impacts on phytoplankton dynamics by free-drifting icebergs in the NW Weddell Sea, *Deep Sea Res., Part II*, 58(11–12), 1422–1435.
- Vernet, M., et al. (2012), Islands of ice: Influence of free-drifting Antarctic icebergs on pelagic marine ecosystems, *Oceanography*, 25(3), 38–39.
- Wadhams, P., M. Kristensen, and O. Orheim (1983), The response of Antarctic icebergs to ocean waves, *J. Geophys. Res.*, 88, 6053–6065.
- Wagner T. J. W., P. Wadhams, R. Bates, P. Elosegui, A. A. Stern, D. Vella, E. P. Abrahamsen, A. Crawford, and K. W. Nicholls (2014), The “foot-loose” mechanism: Iceberg decay from hydrostatic stresses, *Geophys. Res. Lett.*, 41, 5522–5529, doi:10.1002/2014GL060832.
- White, F. M., M. L. Spaulding, and L. Gominho (1980), Theoretical estimates of the various mechanisms involved in iceberg deterioration in the open ocean environment, Ft. Belvoir Defense Technical Information Center, Fort Belvoir, Va. *Tech. Rep. USCG-D-62-80*.
- White, L., E. Deleersnijder, and V. Legat (2008), A three-dimensional unstructured mesh finite element shallow-water model, with application to the flows around an island and in a wind-driven, elongated basin, *Ocean Model.*, 22, 26–47.
- Wolanski, E., T. Asaeda, A. Tanaka, and E. Deleersnijder (1996), Three-dimensional island wakes in the field, laboratory experiments and numerical models, *Cont. Shelf Res.*, 16, 1437–1452.

Erratum

In the originally published version of this article, the figures were incorrectly ordered. The ordering has since been corrected, and this version may be considered the authoritative version of record.